Dalton Transactions

ROYAL SOCIETY OF CHEMISTRY

PAPER

View Article Online
View Journal | View Issue

Cite this: *Dalton Trans.*, 2024, **53**, 14246

Structure and phase changes of alumina produced by flame hydrolysis†

Jamal Nasir,[a] Franz Schmidt,[b] Frank Menzel[b] and Jörn Schmedt auf der Günne *[a]

Received 21st June 2024,
Accepted 29th July 2024

DOI: 10.1039/d4dt01809e

rsc.li/dalton

Fumed alumina from the combustion of $AlCl_3$ produced nano particles with specific areas from 30 to 220 $m^2\ g^{-1}$ (BET) which were characterized by powder X-ray diffraction, ^{27}Al solid-state NMR and transmission electron microscopy. During the short-lived synthesis, highly disordered γ-alumina progressively transforms into a mixture of δ and θ-alumina. For the γ-alumina particles, only for particles with the highest specific area a significant amount of five-coordinated Al can be found which is only partially located in the particle surface. Water can be bound reversibly and increases the coordination number of aluminium atoms in the particle surface. For the well-crystallized mixture of δ and θ-alumina, high resolution and high S/N powder XRD pattern features a large number of superstructure reflections along with the commonly observed diffuse reflections. ^{27}Al MQMAS NMR provides a total of 8 crystallographic sites with an unusually high resolution in the tetrahedral region, with 4 distinct AlO_4 sites pertaining to the δ phase alone. The results suggest that the δ-alumina phase produced in this process can be described as an ordered structure.

Introduction

Combustion of metal and silicon chlorides in an oxyhydrogen flame is an important industrial process for the production of nano-scale oxides including nano-scale alumina particles.[1–3] In a fast process,[3–5] the gas-phase synthesis is understood as a sequence of steps including nucleation and condensation of primary particles, their subsequent collision and coalescence to form homogeneous bigger particles and their aggregation and agglomeration (Fig. 1). The product particles consist of spherical particles joined into bigger objects of a fractal nature.[6]

For the production of nano-scale alumina different flame combustion processes with different starting materials have been investigated.[3] Here we focus on the combustion of $AlCl_3$ in the flame of an oxyhydrogen burner with an adiabatic flame temperature of about 2250 °C because of its industrial relevance. $AlCl_3$, with a sublimation point of 180 °C, is vaporized in the flame and in an exothermic reaction converted into aluminium oxide, which results in the following total reaction.

$$2AlCl_3 + 3H_2 + 1.5O_2 \rightarrow Al_2O_3 + 6HCl \quad (1)$$

So far, aggregated nanostructured materials from this process with a BET surface area up to 150 $m^2\ g^{-1}$ have been reported.[7] Information about the particle size distribution of the primary particles is rather limited but particles in the range from 3 to 200 nm for alumina particles have been estimated from transmission electron micrographs.[8–10] A characterization of products from the combustion process over the complete available range of conditions, that is, with different average particle size, has not been presented yet.

For fumed alumina particles an impressive list of applications is known. The older applications have been reviewed by Pratsinis.[3] Recently, in context with the Li-ion battery formation of a solid-electrolyte interface for a cathode material could be realized by coating with nano-scale alumina particles.[11–14] It is evident that the formed lithium aluminium oxides depend significantly on the type of alumina chosen, *i.e.* the results of fumed alumina with a high specific area of about 130 $m^2\ g^{-1}$ are different from those of 65 $m^2\ g^{-1}$. Moreover, it could be shown that the separator-foil used in modern Li-ion batteries can profit from the addition of fumed alumina particles to reduce the risk of shrinking in case of thermal runaway.[15] An important aspect in Li-ion battery applications is the careful exclusion of humidity to prevent the battery from decompo-

[a]*University of Siegen, Faculty IV: School of Science and Technology, Department of Chemistry and Biology, Inorganic Materials Chemistry and Center of Micro- and Nanochemistry and Engineering (Cμ), Adolf-Reichwein-Straße 2, D-57076 Siegen, Germany. E-mail: gunnej@chemie.uni-siegen.de*
[b]*Evonik, Operations GmbH, Rodenbacher Chaussee 4, D-63457 Hanau, Germany*
† Electronic supplementary information (ESI) available. See DOI: https://doi.org/10.1039/d4dt01809e

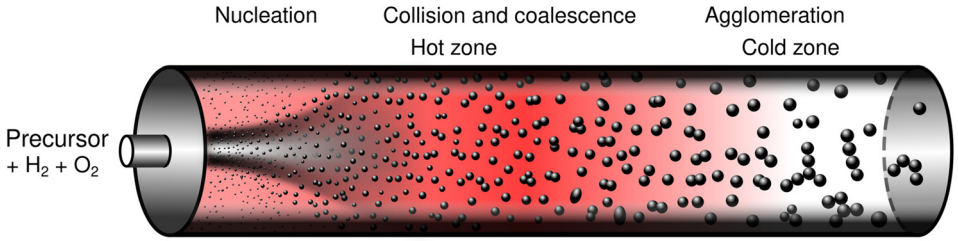

Fig. 1 Processes occurring in the flame combustion synthesis of alumina in the flame of an oxyhydrogen burner when feeding the precursor $AlCl_3$.[4,5]

sition reactions and the ability of nano-scale alumina to act as HF scavengers.[16] Commercially used are currently alumina with a specific area of about 60 to 120 $m^2\ g^{-1}$.[17–21] The question arises in which way the fumed alumina are different apart from the chosen specific surface area. Are there, for example, as well differences in the structure on an atomic scale?

For the atomic structure of the as-synthesized particles *via* the $AlCl_3$ flame combustion process, different crystalline transition alumina phases have been observed by X-ray diffraction,[10,22] including γ-, δ- and α-alumina but the sequence appearance within the flame cooling process is not fully clear. Agreement exists on the γ-phase appearing for high-temperature flames and the δ- and α-phases in the other extreme,[10] which matches observations *via* completely different synthesis routes.[23]

The transition aluminas which can be found under these conditions generally have a much lower density of about 3.6 g cm^{-3} than corundum with 3.98 g cm^{-3}.[24,25] Following Ostwald's step rule, initially the most unstable phase, which is γ-alumina, is expected according to the studies of other synthetic routes for the formation of transition aluminas.[20,21,26,27] This phase is highly disordered on the Al site, while the O-atoms form a cubic closely packed arrangement and feature tetrahedrally and octahedrally coordinated Al atoms.[21,28] While in principle many transition aluminas have been reported,[20,21] relevant to this contribution are only δ-/θ-alumina, which for example can be found upon thermal treatment of boehmite γ-AlOOH.[29,30]

$$\gamma\text{-AlOOH} \rightarrow \gamma \rightarrow \delta \rightarrow \theta \rightarrow \alpha\text{-}Al_2O_3 \quad (2)$$

The structure of δ-alumina is still under discussion,[21,31,32] though a related structure, ω-alumina, could be described as an ordered structure with 9 Al sites in the orthorhombic system.[33] The structure solution of δ-alumina is complicated by intergrowth processes between different structures similar to ω-alumina. What is clear is that both the δ- and the related γ-alumina possess a cubic closed packed O sublattice and tetrahedrally (AlO_4) and octahedrally (AlO_6) coordinated Al atoms.[29,30,34] From the structure of ω-Al_2O_3, δ-alumina can be expected to have a ratio of AlO_4/AlO_6 of approximately 3/5.[33] The next step in the transformation is the formation of θ-alumina, which can be described as an ordered crystal structure in the monoclinic system with two Al sites one tetrahedrally and one octahedrally coordinated.[25,35]

A tool to study the uncertainty in the coordination number of the transition aluminas is solid-state nuclear magnetic resonance (NMR), which is inherently quantitative, element-selective and probes both crystalline and amorphous environments,[36–38] which in the context of heavily disordered or potentially disordered particles produced *via* flame combustion is an advantage in order to produce a representative picture. With respect to the different alumina polymorphs only recently a thorough review of the NMR literature has been published,[39] including computed and experimental values for isotropic chemical shift δ_{iso} and the quadrupole interaction. A particularly useful aspect of NMR is the unambiguous detection of the coordination number including pentacoordinated Al at the γ-alumina surface.[37,40,41]

The target of this contribution is to reach a better understanding of the transformation of transition aluminas in the combustion synthesis of alumina nano-particles from $AlCl_3$ to generate a reliable basis for applications of fumed alumina, for example in the field of battery materials or as a reactive form of aluminium oxide.

Experimental part

Materials

All alumina samples were derived from $AlCl_3$ in hydrogen-air flame.

Synthesis of fumed alumina

$AlCl_3$ was used as the source of Al^{3+} ions, converted into gas phase and fed into oxyhydrogen flame as a homogeneous gas mixture with H_2, O_2, and the carrier gas. The vaporized $AlCl_3$ was transformed into fumed alumina through hydrolysis at high temperatures in the oxyhydrogen flame ($2H_2 + O_2 \rightarrow 2H_2O$) according to the already mentioned reaction (Fig. 2).

Formed in flame residence times between 10 and 100 ms, the fumed alumina particles were in a mixed state with hot gases. Residence times were estimated for the used setup by time-resolved sampling with a pneumatic piston at different positions. The aerosol was then cooled before the solid particles were separated from the corrosive gas. In the final step,

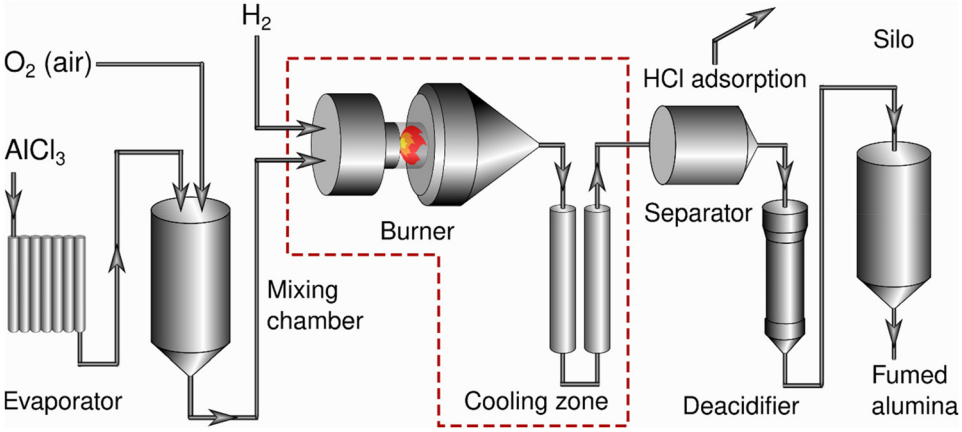

Fig. 2 Experimental setup for the synthesis of fumed alumina from $AlCl_3$ using an oxyhydrogen burner. Burner and cooling zone form a unit. Cooling is achieved through the wall of a water-cooled tubing system. Gaseous HCl is separated from the solid fraction, which depending on particle size for example happens in a cyclone, and then the solid fraction is deacidified by washing with water.

surface HCl was removed and high purity aluminium oxide was obtained.

BET surface area

Triple-point Brunauer–Emmett–Teller (BET) measurements were conducted within the partial pressure region p/p_o of 0.05 to 0.3 with N_2 gas against a certified reference material in order to determine the specific surface area of alumina nanostructured particles. Prior to analysis, the samples were degassed for 20 min under vacuum at 150 °C. The BET analysis was carried out in a certified laboratory in accordance with DIN/ISO9277:2010.

TEM

TEM images of fumed alumina were recorded *via* a field emission high-resolution transmission electron microscope Jeol 2010F (JEOL, Japan) using acceleration voltage of 200 kV. The particles were dispersed in 50 : 50 v.% distilled water and isopropanol solution and afterwards dropped on a copper TEM grid following a drying step at room temperature for 30 min. The arithmetic mean of the diameter of the primary particles were determined from about 2000 individual particles (histograms: Fig. S7†).

Solid-state NMR

^{27}Al MAS NMR spectra were acquired at 156.393 MHz (14.1 T) on a 3.2 mm Bruker MAS probehead (Bruker Avance Neo NMR spectrometer) at 20 kHz spinning frequency. Unless otherwise specified in the results, a selective 90° pulse of 20 μs was applied with a repetition delay of 8 s, and 1024 scans were accumulated. The ^{1}H resonance of 1% TMS in $CDCl_3$ served as an external secondary reference using the Ξ values for ^{27}Al as reported by IUPAC.[42,43]

^{27}Al multiple-quantum MAS (MQMAS) NMR spectra were also acquired at 156.393 MHz (14.1 T) on the 3.2 mm Bruker MAS probe head at 20 kHz spinning frequency. Three-pulse sequence ^{27}Al triple-quantum MQMAS[44] with a zero-quantum filter[45] and with rotor-synchronized sampling of the indirect dimension was utilized. Hard pulses of duration 4.5 and 1.5 μs for the excitation and conversion of quantum coherences, respectively, were determined by running an optimization experiment, and a 20 μs soft pulse (90°) was determined from ^{27}Al nutation experiments. Repetition delays were between 2 and 8 s depending on T_1 relaxation. Phase cycling involved the States method[46] for acquisition of pure absorption line shapes.

NMR spectral simulations were performed using DMfit software package (V 20230120).[47] Spectra for S220–100 were simulated using Czjzek model and for the S65–30 samples using the 'Q mas 1/2' model as implemented in Dmfit.[47,48]

Powder X-ray diffraction

Powder XRD measurements were carried out on a Huber Guinier powder camera G621 (Rimsting, Germany) in asymmetric transmission configuration. A curved Ge(111) monochromator was used to focus the incident beam and monochromatize it to select only $CuK\alpha_1$ radiation.

Mylar foils (1 μm thick) were mounted on round metallic sample holders. Powder samples were placed on the Mylar foil and a second Mylar foil was placed on top of it (no grease was used to hold the powders tight). The powders trapped between the two foils were pressed to form flat round samples. The pressing was done in order to be able to measure a larger sample volume and increase signal-to-noise ratio as the materials are porous and have low crystallinity. Each round sample was measured repeatedly 16 or 64 times by rotating the sample holder in the plane of the sample step-wise, each time using an exposure time of 12 min. The diffraction images were recorded on a BaFX:Eu-based imaging plate (IP) film.[49] During the measurements, the samples were sliding side-ways in the X-ray beam. The X-ray exposed imaging plate was scanned using Typhoon FLA 7000 scanner (GE Company, USA). All the recorded diffraction images were digitized using the IPreader software and the averaging of 64 scans for S30 and 16 scans

for the rest of the samples was done by a gnuplot tcl-script.[49] Rietveld refinement[50] and other types of line shape analyses were performed using TOPAS-Academic V7 software package.[51]

Results and discussion

The basis of this study is a series of alumina batches of materials from the combustion of $AlCl_3$ which underwent different thermal history. These batches feature different specific surface areas and structure. In the following, first the material morphology is studied by gas adsorption and electron microscopy. Then X-ray diffraction is applied to trace the crystalline phases and finally solid-state NMR is applied to monitor the structural changes on an atomic scale.

Particle morphology

In total eight different batches of alumina nanoparticles were investigated which in the following will be named S30–S220 alumina according to their specific surface areas as measured by gas adsorption. "S220" stands for the batch from the fastest cooling process and has a specific surface area of about 220 $m^2\ g^{-1}$ directly after preparation (see Table 1 for the actual BET values).

The gas adsorption data (Table 1) show the expected scaling of the surface area a_S which for perfectly spherical nanoparticles should be inversely proportional to the primary particle diameter d and particle density ρ.

$$a_S = 6/(\rho \cdot d)$$

While the trend is well followed, deviations reflect both the changes in morphology, standard deviations and changes in density because of the presence of different transition alumina (see below). The particle diameters (Table 1 and Fig. S7†) as estimated from transmission electron microscopy predict a higher specific surface, but this is because the primary particle diameter from TEM does not encompass agglomeration and aggregation both of which reduce the specific surface. Aggregates and agglomerates appear under ambient conditions as 'snow flakes' of mm to cm range. In water or other solvents high shear forces as *e.g.* by sonication, the aggregate structure can disrupt to smaller aggregates down to d_{50} of 100 nm, forming stable dispersions. In general, the process as suggested for other fumed oxides consisting of nucleation forming small monocrystalline particles, followed by collision and coalescence forming bigger monocrystalline particles and finally aggregation and agglomeration leading to bigger polycrystalline fractal clusters and particles is also followed here. In part all processes happen for each of the presented compounds because the retention time of particles in the flame is described by a distribution because of flame turbulence which can be seen from the TEM pictures in ESI (Fig. S6–S8†). Even for the samples with the highest specific surface area (S180–220) individual bigger (spherical) particles can be found and *vice versa* smaller particles of 3–5 nm for the samples with low surface area (S30, S45) (Fig. 8 and S6, S8†). The smaller particles of around 5 nm size appear to be monocrystalline in high-resolution TEM images (Fig. S8†).

Table 1 Specific areas a_S as determined by N_2 BET gas adsorption measurements and the arithmetic mean of the particle size d from TEM of the fumed aluminas used in this study

Label in manuscript	$a_S/(m^2\ g^{-1})$	d/nm	Evonik label
S220	222[a]	5.4 ± 2.2	Alu220 ex
S200	198[a]	5 ± 2.2	Alu200 ex
S180	178	4 ± 1.3	Alu180 ex
S130	122	7 ± 2.8	Alu130
S100	102	8.6 ± 3.6	AluC
S65	62	15 ± 8	Alu65
S45	47	18 ± 9	VP Alu45
S30	32	40 ± 18	Alu30 ex

[a] The particles with specific BET surfaces over 200 $m^2\ g^{-1}$ show a reduction of the specific surface over a period of about half a year.

Crystalline phases

Crystalline phases in S220–30 fumed aluminas were investigated by powder X-ray diffraction (Fig. 3). Generally, with increasing resident time in the flame during the synthesis the crystallinity increases, which is reflected by sharper reflections developing. On the way downwards on Ostwald staircase towards α-Al_2O_3, several changes in crystal structure can be observed including γ, δ, θ-alumina, each of which undergoes transformation into the subsequent phase from bottom to top as γ → (δ and θ) while the α-phase could not be observed. The observed sequence corresponds to the sequence observed for the crystallization of an alumina melt.[52]

The observed diffraction patterns for the samples from S220–180 demonstrate only broad reflections with various linewidths. The composition of these samples are dominated by γ-alumina, which is evident by comparison to literature data.[29,53] The non-consistency in FWHM as a function of 2θ has also been observed for boehmite-derived γ-alumina reflections and is to some degree obvious in Fig. 3. However, the usually relatively sharp (222) reflection at 39.4° is significantly broadened in the observed patterns and that is an indication of the small size of the crystallites.[54]

In the samples with even lower specific surface, *i.e.* S65 and below, δ-alumina is evident where the typical δ-triplet reflections between 44 and 47° take shape and the major reflection (400) at 66.7° overlapping with γ (440) occurs. Further decrease in BET leads to the appearance of a large number of superstructure δ reflections more in number than already observed in boehmite-derived δ-alumina.[31] The γ (440) reflection ultimately significantly splits into a very sharp θ-alumina and less sharper δ-alumina reflections indicating significant ordering of the θ phase. The results on S65 to 30 samples are consistent with the interpretation that the transformations γ → δ and γ → θ occur in parallel with the former being the faster (this observation is in agreement with the NMR data and is discussed also under NMR spectral simulations below).

The Rietveld refinement of the γ-phase in S220, S200 and S180 can be achieved using the spinel model with some non-

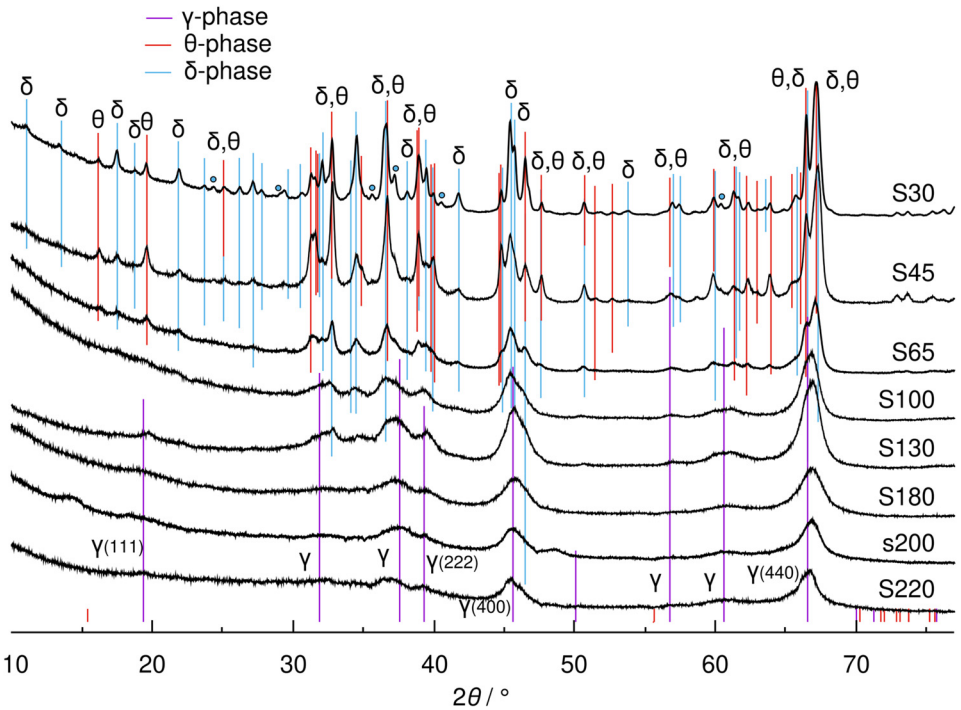

Fig. 3 Powder XRD patterns of fumed alumina samples for S220–30. Three reference diffractograms γ-alumina (Fd3mZ),[15] δ-alumina (P222),[56] and θ-alumina (C12/m1)[10] are shown as color coded vertical lines. The heights of the vertical lines do not correspond to the actual relative intensities but rather serve as visual guide, and some of the lines are deleted for the purpose of better visibility. The blue circles mark reflections non-existent in the δ model.

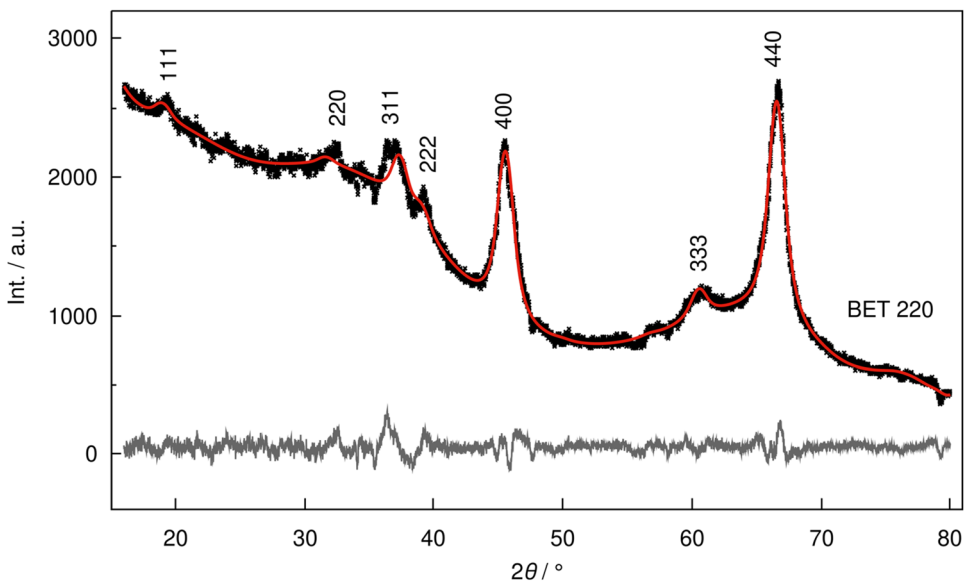

Fig. 4 Rietveld refinement of S220 sample using Smrcok *et al.* for γ alumina with a significant amount of non-spinel occupation. The black points represent the experimental data, the red solid line the calculated diffractogram with a residual profile factor of R_{wp} = 3.6%, and the grey line the difference. The input file is given in the ESI in Table S1.†

spinel occupation of Smrčok *et al.* (Fig. 4 and S1†).[30] The Rietveld refinement, however, requires the occupancy of the non-spinel sites to be significantly higher than the boehmite-derived γ-alumina of Smrcok. While in Smrcok's refinement only 6.3% of all the non-spinel 16c and 48f sites are occupied by Al cations, in the fumed alumina the same type of occupancy reaches around 39%, 30% and 36% in S220, S200 and S180, respectively. The tetrahedral : octahedral relative occu-

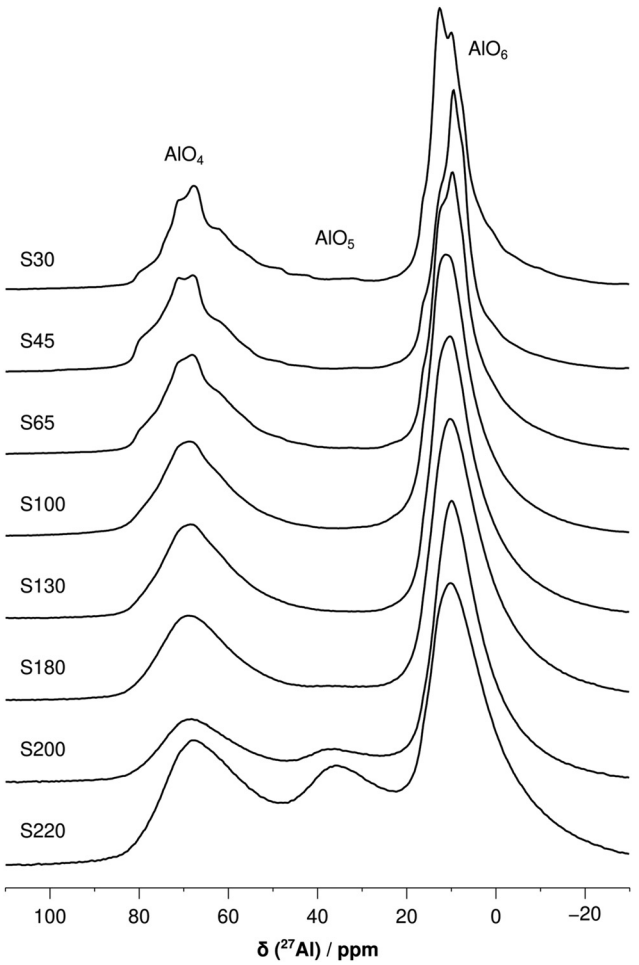

Fig. 5 ^{27}Al MAS NMR spectra of fumed alumina for the S220–30 samples measured at 20 kHz spinning frequency.

pation (64% : 36%, 60% : 40% and 64% : 36%, respectively) remained relatively close to literature values of boehmite-derived γ-alumina. Fitting the occupancy of O (32e) gave values very close to 1 and did not affect the overall refinement. All the Al–O bond distances remained within 0.03% of those of Smrcok's model. While the overall fit looks convincing there is a clear disagreement with the tetrahedral : octahedral relative occupation (see below), which either indicates the presence of a significant amount of amorphous side-phase or a deficiency of the structural model.

The crystallite size obtained using integral breath approach by Rietveld refinement gave for the γ-alumina in the S220, S200 and S180 samples values of 8.2 ± 0.7, 8 ± 0.6 and 6 ± 0.2 nm, respectively. In comparison, the mean values for TEM-derived particle diameter for the same samples are 5.4, 5 and 4 nm, respectively. Given the non-monodisperse distribution of particle sizes (Fig. S6 and S8†), which have an impact on the analysis of the data from both TEM and XRD, this can be interpreted as a rough agreement meaning that crystallite and particle size are approximately the same (see Fig. 8 and S8† for TEM images).

Local structure by ^{27}Al solid-state NMR

^{27}Al MAS NMR provides information about the coordination number and frequency of the corresponding Al environment and for well-crystallized materials information about the number of Al sites can be obtained besides.

The ^{27}Al MAS NMR spectra of (non-dehydrated) fumed alumina provide a consistent decrease in disorder and increase in crystallinity with increasing particle size (bottom to top, Fig. 5), which is evident from the reduction of peak widths. This pattern across the samples agrees with the observations made from powder XRD. The samples with the highest specific surface area show a 2nd order quadrupolar broadened line-shape with a tail, typical of disordered phases, which gradually sharpen and transform into a typical 2nd order quadrupolar line-shape in ordered state.

The S220 sample, mainly consisting of γ phase, shows three Al coordination AlO_4, AlO_5 and AlO_6 with relative intensities of 30.1%, 21.5% and 48.4%, respectively (Fig. S2†). This observation is not agreeing with the results from the refinement of the powder X-ray pattern with Smrcok's model, which suggests that the tetrahedrally coordinated Al environment AlO_4 should be dominant. Furthermore, a significant relative amount AlO_5 is observed.

Moving to the samples with lower specific surface area, the AlO_5 content drastically decreases to 8.6% in S200, less than 2% in S180, and to an unmeasurable amount beyond. The total intensities of AlO_4 and AlO_6 in Fig. 5 do not change monotonically but roughly have plateau from S130 to S30 (see also Fig. 7).

The ^{27}Al MAS measurements on the samples S220, S200, S180 and S130 kept under ambient conditions were repeated after 7 to 13 months with the same acquisition parameters, and the relative intensities and line-shapes remained almost the same (Fig. S5†). This indicates that the samples under ambient conditions are not subject to ageing.

Two possible explanations for this observation are the presence of an amorphous side-phase besides the crystalline γ-alumina and the stabilization of AlO_5 at the surface of γ-alumina which may also explain the observed change in the ratio of tetrahedrally and octahedrally coordinated Al atoms. What can be ruled out is that the surface alone is responsible for the stabilization of AlO_5 because the decay of the relative amount of AlO_5 is too fast (Fig. 7) for the expected antiproportional scaling with the particle diameter. The AlO_4 and AlO_6 resonances in the spectra of the S30 and S45 samples in Fig. 5 are a superposition of different resonances with a small chemical shift difference. Therefore, the MQMAS experiment was applied to achieve a better spectral resolution over the complete sample series.

For the samples from high to low specific surface area, the ^{27}Al MQMAS spectra of fumed alumina show consistent line-narrowing and appearance of distinct resonances (Fig. S3†). The spectrum of the sample S220 shows three distinct sites – AlO_4, AlO_5 and AlO_6 – each of which has very broad distribution both in the direct and isotropic triple-quantum dimen-

sions. The lack of line-narrowing in the isotropic dimension in the S220 and the next samples is evidence of large chemical shift distribution due to extensive disorder. From the sample S130 and onward, the AlO_5 resonance disappears, and distinct peaks belonging to the sites of an ordered crystal structure can be resolved. From sample S100 and onward in the AlO_4 region of the spectrum three sites can be resolved. What these results indicate is that the samples are subject to a series of phase transitions which transform the complete grain.

For the samples with low specific surface area S45 and 30, MQMAS provided indeed a very high resolution which clearly evidences multiple distinct resonances (Fig. 6 and Fig. S3†). The MQMAS spectrum of the sample S30 rendered an unusual high resolution of five distinct tetrahedral resonances alone. In the high-field corner of the same spectrum (Fig. 6a), at least three AlO_6 resonances are recognizable in the isotropic dimension.

The pattern of phase transformations over all the samples can be clearly seen in the isotropic MQMAS projections which also shows a good agreement with the X-ray diffraction data, especially the changes in the tetrahedral region (Fig. S4†), which also reflect the high crystallinity of the compounds of low specific surface area (Fig. 6).

Spectral simulations of ^{27}Al MAS data

In order to obtain a more quantitative description of the processes happening in the fumed alumina particles and the peaks which could be assigned to δ and θ alumina, the ^{27}Al NMR spectra were simulated. The MQMAS spectra and their projections on the isotropic dimension (Fig. S4†) qualitatively helped to simulate the ^{27}Al MAS spectra (the extracted spectral parameters are reported in Table 2, and for all the samples in Table S2†). The MAS spectra of the highly disordered samples (S220 to S100) were simulated using the Czjzek model as implemented in the DMfit software,[47,48] and the chemical shift values for the AlO_4, AlO_5 and AlO_6 sites were determined at around 75, 42 and 15 ppm, respectively. For the samples with BET <100 $m^2\ g^{-1}$, quadrupolar central transition model was used with which the two high-temperature transition aluminas, δ and θ, could be analysed. Despite the high resolution of the MQMAS spectra of S30 and S45 samples, two of the five AlO_4 resonances could not be fitted because of low signal to noise. Nevertheless, a total of six resonances (3 × AlO_4 and 3 × AlO_6) were fitted to each of these spectra (Fig. 6b, S2,† Table 2 and Table S2†). In the series of measured ^{27}Al MQMAS spectra, the unprecedented resolution reached in S30 (Fig. 6a) shows that the crystallization has developed to the extent that both δ- and θ-alumina can be considered as ordered phases. The AlO_4 signal region of the sample S30 contains only well-resolved isotropic resonances both for δ-alumina (four distinct resonances) and θ-alumina (one distinct resonance) which means that both structures cannot be disordered.

The well-defined quadrupolar shape of the tetrahedral line in the θ phase[36] was useful in the fitting procedure and made the entire fit more reliable; a rough 1 : 1 ratio of AlO_4 : AlO_6 integrated intensity was imposed. Integrating the models gave a higher θ-alumina content in the sample S45 (54%) than in the sample S30 (34%). Three types of measurements – XRD, MAS NMR and MQMAS – consistently show the highest θ intensity in S45 in all the samples. Therefore, two transformations, γ → δ and γ → θ, are apparently occurring in parallel.

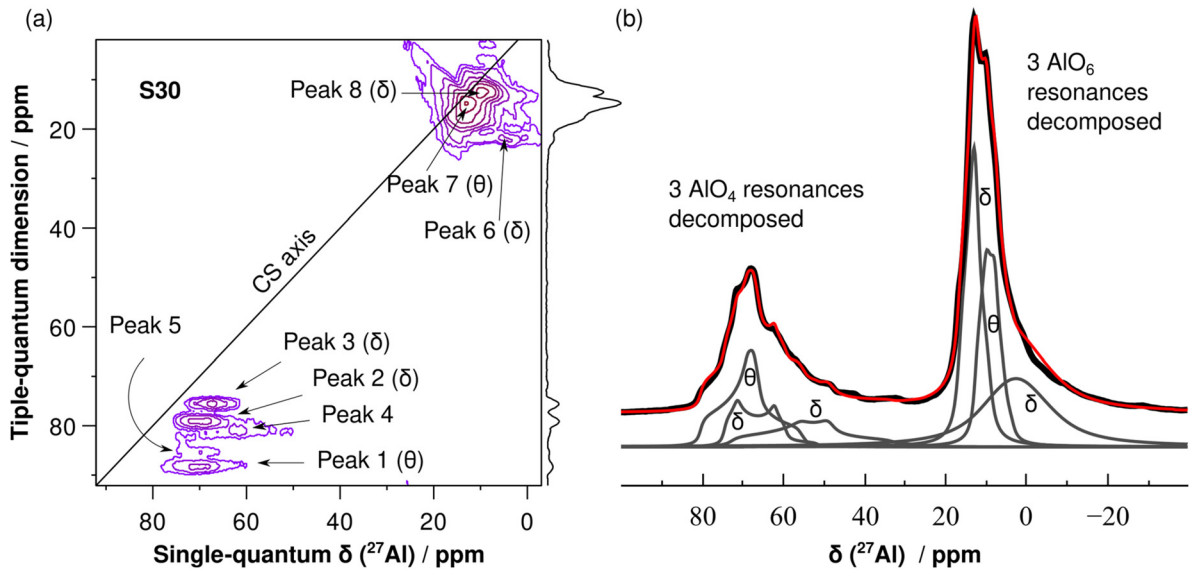

Fig. 6 (a) Sheared ^{27}Al triple-quantum MQMAS NMR spectrum of fumed alumina for S30. (b) ^{27}Al MAS and simulated spectrum using quadrupolar central transition model. The measurements are carried out 20 kHz MAS frequency. In (b) the experimental data are shown in black, the total simulated spectra in red, and the individual decomposed spectra in grey. The assignments in the MQMAS spectra are done following the simulations of the 1D spectra.

Table 2 ^{27}Al MAS NMR parameters for the AlO_4, AlO_5 and AlO_6 sites in fumed alumina materials obtained by using DMfit package and the corresponding literature values (complete table for all the samples are given in Table S2†)

Sample label	Main phase	Type	δ_{iso}/ppm	C_Q/MHz	η	Model used	Relative intensities	Comment
	γ-Al_2O_3	AlO_4	77.5 ± 0.2	3.5 ± 0.1		Czjzek	10%	DNP NMR[55]
		AlO_5	37.2 ± 0.2	4.5 ± 0.1			13%	
		AlO_6	14.0 ± 0.2	4.3 ± 0.1			78%	
	δ-Alumina	AlO_4	73.2	4.6	0.6		19.6%	Al isopropoxide precursor; sol–gel[38]
		AlO_4	68.3	6.6	0.4		20.7%	
		AlO_6	16.3	4.8	0.0		25.8%	
		AlO_6	14.5	4.3	0.6		33.9%	
	θ-Alumina	AlO_4	80 (1)	6.4 (0.1)	0.65(0.02)		47.8%	Al tributoxide precursor; sol–gel[36]
		AlO_6	10.5 (1)	3.5 (0.3)	0(0.1)		52.2%	
S220	γ-Alumina	AlO_4	75	6.6		Czjzek	30.1%	This study
		AlO_5	42	6.2			21.5%	
		AlO_6	15.3	5.6			48.4%	
S30	θ-Alumina	AlO_4	80.4	6.1	0.9	Q mas 1/2	15.6%	This study
		AlO_6	12.7	3.9	0.5		18.3%	
	δ-Alumina	AlO_4	76.6	6.4	0.2		8%	
		AlO_4	73.3	8.3	0.7		9%	
		AlO_6	16.4	3.3	1		24.1%	
		AlO_6	10.2	5.2	0.7		25%	

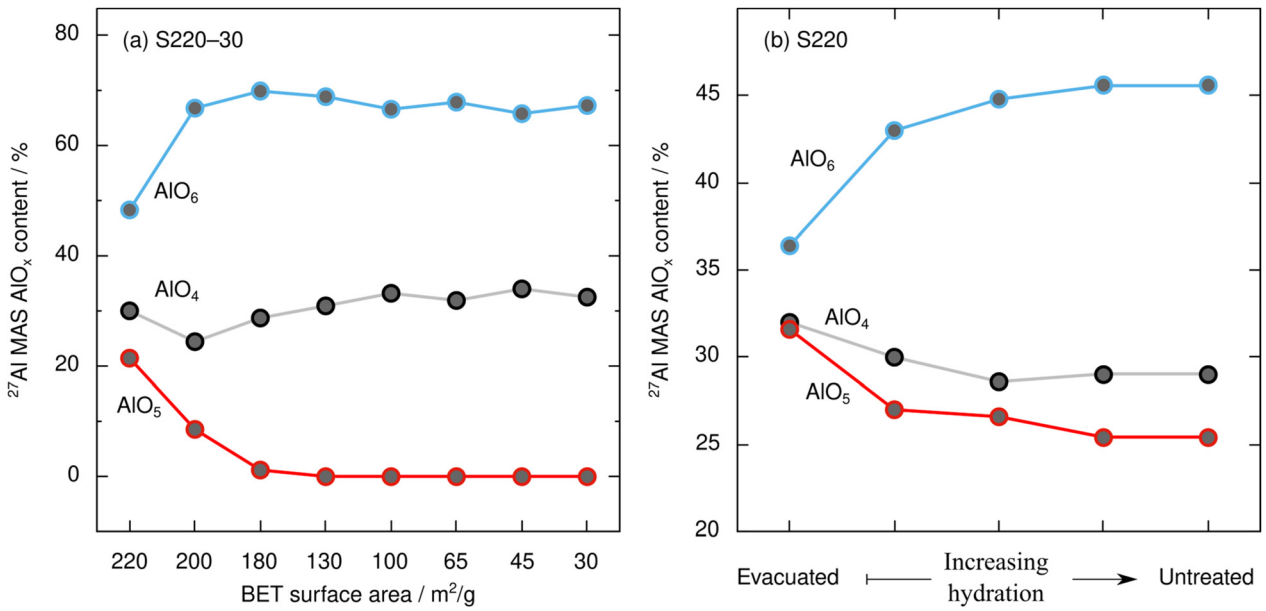

Fig. 7 (a) AlO_4, AlO_5 and AlO_6 contents in the S220–30 fumed alumina samples measured by ^{27}Al MAS NMR and (b) after low-vacuum evacuation at 300 °C for 2 days of the sample and rehydroxylation/rehydration of the samples step-by-step inside the rotor after each measurement. The spectra were acquired using a 30° tip angle at 100 kHz nutation frequency.

De-/rehydration experiments and structural model

To get a better understanding of the sample surface the samples were exposed to vacuum at 295 K, which leads to a partial dehydration of the sample surface. After the evacuation, the sample S220 was transferred in a Schlenk finger into a glovebox where it was packed in 3.2 mm NMR rotor. The first ^{27}Al MAS measurement was carried out immediately after taking the rotor out of the glovebox; subsequently the rotor cap was kept open overnight before each of the following measurements in order to slowly admit air and rehydrate the material. The measurements show that around 10% of AlO_6 and AlO_5 interconverts (Fig. 7b); a significant interconversion between AlO_5 and AlO_6, however, is not evident in the MAS measurements. Because re-/dehydration is expected at the surface, it can be concluded that water molecules coordinate the aluminium atoms and upon dehydration cause a change of the coordination number. Note that the condensation of two Al–O–H groups would not cause a change of the coordination number as observed. Because AlO_5 (Fig. 7b) is not completely converted into AlO_6 by rehydration indicates that a significant amount of AlO_5 is not directly at the particle surface.

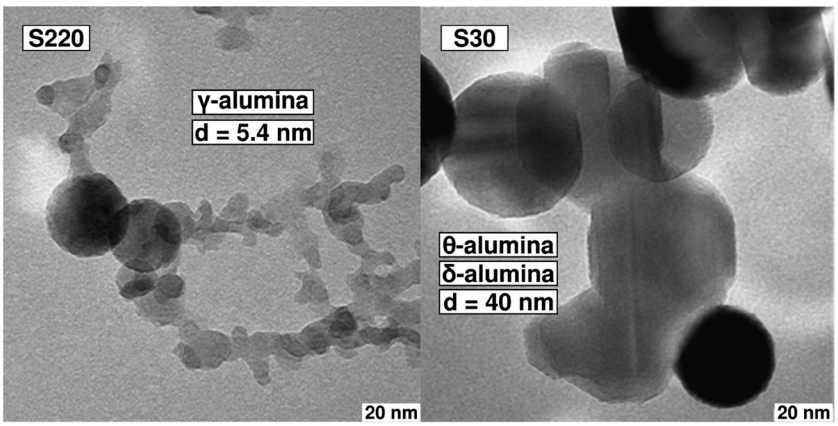

Fig. 8 TEM images of S220 (left) and S30 (right) fumed alumina samples. The S220 sample, mainly γ-alumina, undergoes a transformation pathway as γ → δ, θ leading to well-crystalline δ and θ-alumina in S30.

Conclusions

Fumed alumina produced in the combustion of $AlCl_3$ can be assorted into three different classes of nano-particles. Particles with the highest surface area (≥180 m^2 g^{-1}) and smallest particle size are highly disordered and show reflections of γ-alumina but also fivecoordinate aluminium which is only partially localized at the particle surface. These particles show a reversible binding of water which converts the coordination number of the surface aluminium atoms and makes them suitable for catching water in the corresponding applications. When the combustion is controlled so that particles with lower specific surface area (≥130 m^2 g^{-1}) are formed, then the amount of fivefold coordinate aluminium is significantly reduced while still showing the reflections of the γ-phase. For even bigger particles sizes and smaller specific surface area the transition alumina phases of δ and θ can be observed. The γ → δ ordering starts earlier and proceeds faster than the γ → θ transformation which leads to both the δ and θ becoming ordered phases. Although powder XRD data showed relatively sharp reflections, it was mainly ^{27}Al MQMAS NMR that provided evidence for the ordered nature of both δ and θ, giving an impressive four distinct peaks for the tetrahedral sites in δ-alumina alone. The results indicate that fumed alumina with high specific surface area may be excellent precursors for ceramics and as a reactive form of aluminium oxide, but a significant amount of water is bound to the corresponding surfaces.

Author contributions

Formal analysis: J. N.; investigation: J. N., F. S., F. M.; writing – original draft: J. N.; visualization: J. N., F. M., F. S.; project administration: J. S. A. D. G.; conceptualization: J. S. A. D. G.; writing – review & editing: J. S. A. D. G.; supervision: J. S. D. A. G.

Data availability

We have prepared a detailed and extensive set of plots and compiled that in the ESI.†

Data can be made available upon request.

Conflicts of interest

There are no conflicts to declare.

Acknowledgements

We dedicate this work to the late Dr Johannes Weber.

References

1 H. Kloepfer, Verfahren zum Reinigen von hochdispersen Oxyden von Metallen bzw, DE762723A, 1952, Metalloiden.
2 M. S. Wooldridge, Gas-Phase Combustion Synthesis of Particles, *Prog. Energy Combust. Sci.*, 1998, **24**(1), 63–87, DOI: 10.1016/S0360-1285(97)00024-5.
3 S. E. Pratsinis, Flame Aerosol Synthesis of Ceramic Powders, *Prog. Energy Combust. Sci.*, 1998, **24**(3), 197–219, DOI: 10.1016/S0360-1285(97)00028-2.
4 R. N. Grass, S. Tsantilis and S. E. Pratsinis, Design of High-temperature, Gas-phase Synthesis of Hard or Soft TiO_2 Agglomerates, *AIChE J.*, 2006, **52**(4), 1318–1325, DOI: 10.1002/aic.10739.
5 S. E. Pratsinis and S. Vemury, Particle Formation in Gases: A Review, *Powder Technol.*, 1996, **88**(3), 267–273, DOI: 10.1016/S0032-5910(96)03130-0.
6 L. S. Vikulina, A. V. Nomoev and A. Y. Godymchuk, Determining the Degree of Nanopowders Hydrophilicity by the Ratio Fractal Dimension to the Specific Surface, *Adv.*

Mater. Res., 2015, **1085**, 44–49, DOI: 10.4028/www.scientific.net/AMR.1085.44.

7 V. I. Zarko, V. M. Gun'ko, E. Chibowski, V. V. Dudnik and R. Lèboda, Study of Surfaces Properties of Fumed Alumina/Silica Materials., *Colloids Surf., A*, 1997, **127**(1–3), 11–18, DOI: 10.1016/S0927-7757(97)00021-6.

8 M. Sokolowski, A. Sokolowska, A. Michalski and B. Gokieli, The "in-Flame-Reaction" Method for Al_2O_3 Aerosol Formation, *J. Aerosol Sci.*, 1977, **8**(4), 219–230, DOI: 10.1016/0021-8502(77)90041-6.

9 P. Albers, M. Maier, M. Reisinger, B. Hannebauer and R. Weinand, Physical Boundaries within Aggregates – Differences between Amorphous, Para–crystalline, and Crystalline Structures, *Cryst. Res. Technol.*, 2015, **50**(11), 846–865, DOI: 10.1002/crat.201500040.

10 G. D. Sextl, H. D. Swarowsky, M. Koerfer, P. D. Kleinschmit and R. D. Schwarz, (Alpha)-Aluminiumoxid und Verfahren zu seiner Herstellung, DE4009299A1, 1990.

11 M. J. Herzog, N. Gauquelin, D. Esken, J. Verbeeck and J. Janek, Facile Dry Coating Method of High–Nickel Cathode Material by Nanostructured Fumed Alumina (Al_2O_3) Improving the Performance of Lithium–Ion Batteries, *Energy Technol.*, 2021, **9**(4), 2100028, DOI: 10.1002/ente.202100028.

12 M. J. Herzog, D. Esken and J. Janek, Improved Cycling Performance of High–Nickel NMC by Dry Powder Coating with Nanostructured Fumed Al_2O_3, TiO_2, and ZrO_2: A Comparison, *Batteries Supercaps*, 2021, **4**(6), 1003–1017, DOI: 10.1002/batt.202100016.

13 M. J. Herzog, N. Gauquelin, D. Esken, J. Verbeeck and J. Janek, Increased Performance Improvement of Lithium-Ion Batteries by Dry Powder Coating of High-Nickel NMC with Nanostructured Fumed Ternary Lithium Metal Oxides, *ACS Appl. Energy Mater.*, 2021, **4**(9), 8832–8848, DOI: 10.1021/acsaem.1c00939.

14 Y. Chen, Y. Zhang, F. Wang, Z. Wang and Q. Zhang, Improve the Structure and Electrochemical Performance of $LiNi_{0.6}Co_{0.2}Mn_{0.2}O_2$ Cathode Material by Nano-Al_2O_3 Ultrasonic Coating, *J. Alloys Compd.*, 2014, **611**, 135–141, DOI: 10.1016/j.jallcom.2014.05.068.

15 J. H. Ahn, T.-S. You, S.-M. Lee, D. Esken, D. Dehe, Y.-C. Huang and D.-W. Kim, Hybrid Separator Containing Reactive, Nanostructured Alumina Promoting *in situ* Gel Electrolyte Formation for Lithium-Ion Batteries with Good Cycling Stability and Enhanced Safety, *J. Power Sources*, 2020, **472**, 228519, DOI: 10.1016/j.jpowsour.2020.228519.

16 Z. Chen, Y. Qin, K. Amine and Y.-K. Sun, Role of Surface Coating on Cathode Materials for Lithium-Ion Batteries, *J. Mater. Chem.*, 2010, **20**(36), 7606, DOI: 10.1039/c0jm00154f.

17 V. M. Gun'ko, V. I. Zarko, O. V. Goncharuk, A. K. Matkovsky, O. S. Remez, J. Skubiszewska-Zięba, G. Wojcik, B. Walusiak and J. P. Blitz, Nature and Morphology of Fumed Oxides and Features of Interfacial Phenomena, *Appl. Surf. Sci.*, 2016, **366**, 410–423, DOI: 10.1016/j.apsusc.2016.01.062.

18 V. M. Gun'ko, Y. M. Nychiporuk, V. I. Zarko, E. V. Goncharuk, O. A. Mishchuk, R. Leboda, J. Skubiszewska-Zięba, E. Skwarek, W. Janusz, G. R. Yurchenko, V. D. Osovskii, Y. G. Ptushinskii, V. V. Turov, P. P. Gorbik, J. P. Blitz and K. Gude, Relationships between Surface Compositions and Properties of Surfaces of Mixed Fumed Oxides, *Appl. Surf. Sci.*, 2007, **253**(6), 3215–3230, DOI: 10.1016/j.apsusc.2006.07.013.

19 H. Pines and W. O. Haag, Alumina: Catalyst and Support. I. Alumina, Its Intrinsic Acidity and Catalytic Activity, *J. Am. Chem. Soc.*, 1960, **82**(10), 2471–2483, DOI: 10.1021/ja01495a021.

20 K. Wefers and C. Misra, Oxides and Hydroxides of Aluminum, in *Alcoa Technical Paper No. 19*; Alcoa Research Laboratories, 1987, pp. 1–92.

21 I. Levin and D. Brandon, Metastable Alumina Polymorphs: Crystal Structures and Transition Sequences, *J. Am. Ceram. Soc.*, 2005, **81**(8), 1995–2012, DOI: 10.1111/j.1151-2916.1998.tb02581.x.

22 M. Formenti, F. Juillet, P. Meriaudeau, S. J. Teichner and P. Vergnon, Preparation in a Hydrogen-Oxygen Flame of Ultrafine Metal Oxide Particles. Oxidative Properties toward Hydrocarbons in the Presence of Ultraviolet Radiation, *J. Colloid Interface Sci.*, 1972, **39**(1), 79–89, DOI: 10.1016/0021-9797(72)90144-0.

23 P. Kaur, A. Khanna, N. Kaur, P. Nayar and B. Chen, Synthesis and Structural Characterization of Alumina Nanoparticles, *Phase Transitions*, 2020, **93**(6), 596–605, DOI: 10.1080/01411594.2020.1765245.

24 J. Lewis, D. Schwarzenbach and H. D. Flack, Electric Field Gradients and Charge Density in Corundum, α-Al_2O_3, *Acta Crystallogr., Sect. A: Cryst. Phys., Diffr., Theor. Gen. Crystallogr.*, 1982, **38**(5), 733–739, DOI: 10.1107/S0567739482001478.

25 E. Husson and Y. Repelin, Structural Studies of Transition Aluminas. Theta Alumina, *Eur. J. Solid State Inorg. Chem.*, 1996, **33**, 1223–1231.

26 X. Krokidis, P. Raybaud, A.-E. Gobichon, B. Rebours, P. Euzen and H. Toulhoat, Theoretical Study of the Dehydration Process of Boehmite to γ-Alumina, *J. Phys. Chem. B*, 2001, **105**(22), 5121–5130, DOI: 10.1021/jp0038310.

27 L. Samain, A. Jaworski, M. Edén, D. M. Ladd, D.-K. Seo, F. J. Garcia-Garcia and U. Häussermann, Structural Analysis of Highly Porous γ-Al_2O_3, *J. Solid State Chem.*, 2014, **217**, 1–8, DOI: 10.1016/j.jssc.2014.05.004.

28 A. Boumaza, L. Favaro, J. Lédion, G. Sattonnay, J. B. Brubach, P. Berthet, A. M. Huntz, P. Roy and R. Tétot, Transition Alumina Phases Induced by Heat Treatment of Boehmite: An X-Ray Diffraction and Infrared Spectroscopy Study, *J. Solid State Chem.*, 2009, **182**(5), 1171–1176, DOI: 10.1016/j.jssc.2009.02.006.

29 R.-S. Zhou and R. L. Snyder, Structures and Transformation Mechanisms of the η, γ and θ Transition Aluminas, *Acta Crystallogr., Sect. B: Struct. Sci.*, 1991, **47**(5), 617–630, DOI: 10.1107/S0108768191002719.

30 Ľ. Smrčok, V. Langer and J. Křesťan, γ-Alumina: A Single-Crystal X-Ray Diffraction Study, *Acta Crystallogr., Sect. C: Cryst. Struct. Commun.*, 2006, **62**(9), i83–i84, DOI: 10.1107/S0108270106026850.

31 S. V. Tsybulya and G. N. Kryukova, New X-Ray Powder Diffraction Data on δ-Al_2O_3, *Powder Diffr.*, 2003, **18**(4), 309–311, DOI: 10.1154/1.1604128.

32 L. Kovarik, M. Bowden, D. Shi, J. Szanyi and C. H. F. Peden, Structural Intergrowth in δ-Al_2O_3, *J. Phys. Chem. C*, 2019, **123**(14), 9454–9460, DOI: 10.1021/acs.jpcc.8b10135.

33 G. Wallez, "ω-Al_2O_3" a Microcrystalline Ordered Form of Transition Spinel Alumina Metastable up to 1200 °C, *J. Solid State Chem.*, 2022, **312**, 123303, DOI: 10.1016/j.jssc.2022.123303.

34 L. Kovarik, M. Bowden, A. Genc, J. Szanyi, C. H. F. Peden and J. H. Kwak, Structure of δ-Alumina: Toward the Atomic Level Understanding of Transition Alumina Phases, *J. Phys. Chem. C*, 2014, **118**(31), 18051–18058, DOI: 10.1021/jp500051j.

35 G. Yamaguchi, I. Yasui and W.-C. Chiu, A New Method of Preparing θ-Alumina and the Interpretation of Its X-Ray-Powder Diffraction Pattern and Electron Diffraction Pattern, *Bull. Chem. Soc. Jpn.*, 1970, **43**(8), 2487–2491, DOI: 10.1246/bcsj.43.2487.

36 L. A. O'Dell, S. L. P. Savin, A. V. Chadwick and M. E. Smith, A ^{27}Al MAS NMR Study of a Sol–Gel Produced Alumina: Identification of the NMR Parameters of the θ-Al_2O_3 Transition Alumina Phase, *Solid State Nucl. Magn. Reson.*, 2007, **31**(4), 169–173, DOI: 10.1016/j.ssnmr.2007.05.002.

37 J. Z. Hu, S. Xu, J. H. Kwak, M. Y. Hu, C. Wan, Z. Zhao, J. Szanyi, X. Bao, X. Han, Y. Wang and C. H. F. Peden, High Field ^{27}Al MAS NMR and TPD Studies of Active Sites in Ethanol Dehydration Using Thermally Treated Transitional Aluminas as Catalysts, *J. Catal.*, 2016, **336**, 85–93, DOI: 10.1016/j.jcat.2016.01.006.

38 S. Xu, N. R. Jaegers, W. Hu, J. H. Kwak, X. Bao, J. Sun, Y. Wang and J. Z. Hu, High-Field One-Dimensional and Two-Dimensional ^{27}Al Magic-Angle Spinning Nuclear Magnetic Resonance Study of θ-, δ-, and γ-Al_2O_3 Dominated Aluminum Oxides: Toward Understanding the Al Sites in γ-Al_2O_3, *ACS Omega*, 2021, **6**(5), 4090–4099, DOI: 10.1021/acsomega.0c06163.

39 C. V. Chandran, C. E. A. Kirschhock, S. Radhakrishnan, F. Taulelle, J. A. Martens and E. Breynaert, Alumina: Discriminative Analysis Using 3D Correlation of Solid-State NMR Parameters, *Chem. Soc. Rev.*, 2019, **48**(1), 134–156, DOI: 10.1039/C8CS00321A.

40 J. H. Kwak, J. Hu, D. Mei, C.-W. Yi, D. H. Kim, C. H. F. Peden, L. F. Allard and J. Szanyi, Coordinatively Unsaturated Al^{3+} Centers as Binding Sites for Active Catalyst Phases of Platinum on γ-Al_2O_3, *Science*, 2009, **325**(5948), 1670–1673, DOI: 10.1126/science.1176745.

41 H.-I. Kim and S. K. Lee, Probing the Transformation Paths from Aluminum (Oxy)Hydroxides (Boehmite, Bayerite, and Gibbsite) to Metastable Alumina: A View from High-Resolution ^{27}Al MAS NMR, *Am. Mineral.*, 2021, **106**(3), 389–403, DOI: 10.2138/am-2020-7481.

42 R. K. Harris and E. D. Becker, NMR Nomenclature: Nuclear Spin Properties and Conventions for Chemical Shifts—IUPAC Recommendations, *J. Magn. Reson.*, 2002, **156**(2), 323–326, DOI: 10.1006/jmre.2002.2554.

43 R. K. Harris, E. D. Becker, S. M. Cabral De Menezes, P. Granger, R. E. Hoffman and K. W. Zilm, Further Conventions for NMR Shielding and Chemical Shifts (IUPAC Recommendations 2008), *Pure Appl. Chem.*, 2008, **80**(1), 59–84, DOI: 10.1351/pac200880010059.

44 L. Frydman and J. S. Harwood, Isotropic Spectra of Half-Integer Quadrupolar Spins from Bidimensional Magic-Angle Spinning NMR, *J. Am. Chem. Soc.*, 1995, **117**(19), 5367–5368, DOI: 10.1021/ja00124a023.

45 J.-P. Amoureux, C. Fernandez and S. Steuernagel, ZFiltering in MQMAS NMR, *J. Magn. Reson., Ser. A*, 1996, **123**(1), 116–118, DOI: 10.1006/jmra.1996.0221.

46 D. J. States, R. A. Haberkorn and D. J. Ruben, A Two-Dimensional Nuclear Overhauser Experiment with Pure Absorption Phase in Four Quadrants, *J. Magn. Reson.*, 1982, **48**(2), 286–292, DOI: 10.1016/0022-2364(82)90279-7.

47 D. Massiot, F. Fayon, M. Capron, I. King, S. Le Calvé, B. Alonso, J.-O. Durand, B. Bujoli, Z. Gan and G. Hoatson, Modelling One- and Two-Dimensional Solid-State NMR Spectra: Modelling 1D and 2D Solid-State NMR Spectra, *Magn. Reson. Chem.*, 2002, **40**(1), 70–76, DOI: 10.1002/mrc.984.

48 G. Czjzek, J. Fink, F. Götz, H. Schmidt, J. M. D. Coey, J.-P. Rebouillat and A. Liénard, Atomic Coordination and the Distribution of Electric Field Gradients in Amorphous Solids, *Phys. Rev. B: Condens. Matter Mater. Phys.*, 1981, **23**(6), 2513–2530, DOI: 10.1103/PhysRevB.23.2513.

49 J. Nasir, N. Steinbrück, K. Xu and B. Engelen, Schmedt auf der Günne, J. Digitization of Imaging Plates from Guinier Powder X-Ray Diffraction Cameras, *J. Appl. Crystallogr.*, 2022, **55**(5), 1097–1103, DOI: 10.1107/S160057672200677X.

50 H. M. Rietveld, A Profile Refinement Method for Nuclear and Magnetic Structures, *J. Appl. Crystallogr.*, 1969, **2**(2), 65–71, DOI: 10.1107/S0021889869006558.

51 A. A. Coelho, *TOPAS* and *TOPAS-Academic*: An Optimization Program Integrating Computer Algebra and Crystallographic Objects Written in C++, *J. Appl. Crystallogr.*, 2018, **51**(1), 210–218, DOI: 10.1107/S1600576718000183.

52 V. Jayaram and C. G. Levi, The Structure of δ-Alumina Evolved from the Melt and the $\gamma \rightarrow \delta$ Transformation, *Acta Metall.*, 1989, **37**(2), 569–578, DOI: 10.1016/0001-6160(89)90240-X.

53 B. C. Lippens and J. H. de Boer, Study of Phase Transformations during Calcination of Aluminum Hydroxides by Selected Area Electron Diffraction, *Acta Crystallogr.*, 1964, **17**(10), 1312–1321, DOI: 10.1107/S0365110X64003267.

54 S. V. Tsybulya and G. N. Kryukova, Nanocrystalline Transition Aluminas: Nanostructure and Features of X-Ray

Powder Diffraction Patterns of Low-Temperature Al_2O_3 Polymorphs, *Phys. Rev. B: Condens. Matter Mater. Phys.*, 2008, **77**(2), 024112, DOI: **10.1103/PhysRevB.77.024112**.

55 M. Mais, S. Paul, N. S. Barrow and J. J. Titman, Dynamic Nuclear Polarisation Enhanced Solid-State Nuclear Magnetic Resonance Studies of Surface Modification of γ-Alumina, *Johnson Matthey Technol. Rev.*, 2018, **62**(3), 271–278, DOI: **10.1595/205651318X696765**.

56 D. Fargeot, D. Mercurio and A. Dauger, Structural Characterization of Alumina Metastable Phases in Plasma Sprayed Deposits, *Mater. Chem. Phys.*, 1990, **24**(3), 299–314, DOI: **10.1016/0254-0584(90)90093-P**.